Monthly Notices
of the
ROYAL ASTRONOMICAL SOCIETY

MNRAS **491,** 1398–1407 (2020)
Advance Access publication 2019 November 11

doi:10.1093/mnras/stz3138

Reionization and cosmic dawn astrophysics from the Square Kilometre Array: impact of observing strategies

Bradley Greig [1,2]★ Andrei Mesinger[3] and Léon V. E. Koopmans[4]

[1]*ARC Centre of Excellence for All-Sky Astrophysics in 3 Dimensions (ASTRO 3D), University of Melbourne, VIC 3010, Australia*
[2]*School of Physics, University of Melbourne, Parkville, VIC 3010, Australia*
[3]*Scuola Normale Superiore, Piazza dei Cavalieri 7, I-56126 Pisa, Italy*
[4]*Kapteyn Astronomical Institute, University of Groningen, PO Box 800, NL-9700 AV Groningen, the Netherlands*

Accepted 2019 November 4. Received 2019 October 30; in original form 2019 June 19

ABSTRACT

Interferometry of the cosmic 21-cm signal is set to revolutionize our understanding of the epoch of reionization (EoR) and the cosmic dawn (CD). The culmination of ongoing efforts will be the upcoming Square Kilometre Array (SKA), which will provide tomography of the 21-cm signal from the first billion years of our Universe. Using a galaxy formation model informed by high-z luminosity functions, here we forecast the accuracy with which the first phase of SKA-low (SKA1-low) can constrain the properties of the unseen galaxies driving the astrophysics of the EoR and CD. We consider three observing strategies: (i) deep (1000 h on a single field); (ii) medium-deep (100 h on 10 independent fields); and (iii) shallow (10 h on 100 independent fields). Using the 21-cm power spectrum as a summary statistic, and conservatively *only* using the 21-cm signal above the foreground wedge, we predict that all three observing strategies should recover astrophysical parameters to a fractional precision of $\sim$0.1–10 per cent. The reionization history is recovered to an uncertainty of $\Delta z \lesssim 0.1$ (1σ) for the bulk of its duration. The medium-deep strategy, balancing thermal noise against cosmic variance, results in the tightest constraints, slightly outperforming the deep strategy. The shallow observational strategy performs the worst, with up to an $\sim$10–60 per cent increase in the recovered uncertainty. We note, however, that non-Gaussian summary statistics, tomography, as well as unbiased foreground removal would likely favour the deep strategy.

Key words: galaxies: high-redshift – intergalactic medium – dark ages, reionization, first stars – diffuse radiation – early Universe – cosmology: theory.

1 INTRODUCTION

Observing the growth of astrophysical objects (e.g. stars and galaxies) in the first billion years of cosmic history remains elusive. After recombination, the early Universe is enshrouded in a pervasive fog of neutral hydrogen rendering it opaque to the ultraviolet (UV) light from the primordial galaxies. Over time, these galaxies become more abundant, clustering together around high-density peaks. Eventually, the cumulative output of ionizing radiation from these galaxies will produce ionized (H II) regions in the neutral intergalactic medium (IGM). Percolation of these H II regions through continual star formation and galaxy growth eventually succeeds in almost completely ionizing the IGM, referred to as the epoch of reionization (EoR). Unfortunately, the dominant population of sources responsible for reionization will likely be too faint even for the forthcoming space-based telescopes such as the *James Webb Space Telescope* (JWST) (Gardner et al. 2006; Bouwens et al. 2015a; Mitra, Choudhury & Ferrara 2015).

It is not all doom and gloom though. Prior to the completion of reionization, the sheer abundance of neutral hydrogen will allow us to detect the IGM using the 21-cm spin-flip transition, causing emission or absorption against the cosmic microwave background (CMB; see e.g. Gnedin & Ostriker 1997; Madau, Meiksin & Rees 1997; Shaver et al. 1999; Tozzi et al. 2000; Gnedin & Shaver 2004; Furlanetto, Oh & Briggs 2006; Morales & Wyithe 2010; Pritchard & Loeb 2012). This spatial and frequency (hence also redshift and cosmic time) dependent signal reveals a full three-dimensional movie of the IGM during the early Universe. As it is sensitive to the thermal and ionization state of the cosmic gas, the 21-cm signal will allow us to infer the typical UV and X-ray properties of the (unseen) galaxy population driving astrophysical processes during the EoR and CD.

However, observing the cosmic 21-cm signal is challenging. It is extremely faint, buried roughly five orders of magnitude below bright astrophysical foregrounds. Nevertheless over the previous

★ E-mail: greigb@unimelb.edu.au

decade numerous experiments have sought to statistically detect the signal. These can be broken down into two general categories: (i) large-scale interferometric experiments seeking a measurement of the spatial fluctuations, such as the Murchison Wide Field Array (MWA; Tingay et al. 2013), the Low-Frequency Array (LOFAR; van Haarlem et al. 2013; Yatawatta et al. 2013) and the Precision Array for Probing the EoR (PAPER; Parsons et al. 2010) and (ii) all-sky averaged global signal experiments, such as the Experiment to Detect the Global EoR Signature (EDGES; Bowman & Rogers 2010), the Sonda Cosmológica de las Islas para la Detección de Hidrógeno Neutro (SCI-HI; Voytek et al. 2014), the Shaped Antenna measurement of the background RAdio Spectrum (SARAS; Patra et al. 2015), Broadband Instrument for Global HydrOgen ReioNisation Signal (BIGHORNS; Sokolowski et al. 2015), the Large Aperture Experiment to detect the Dark Ages (LEDA; Greenhill & Bernardi 2012; Bernardi et al. 2016), Probing Radio Intensity at high-Z from Marion (PRI^{Z}M; Philip et al. 2019), and the Netherlands-China Low-Frequency Explorer (NCLE[1]).

Aside from an absorption feature in the global signal near $z \approx 17$ reported by EDGES (Bowman et al. 2018a), whose interpretation continues to be controversial (see e.g. Draine & Miralda-Escudé 2018; Hills et al. 2018; Bowman et al. 2018b; Bradley et al. 2019; Singh & Subrahmanyan 2019), existing experiments have thus far only been able to achieve upper limits on the global 21-cm signal (Bernardi et al. 2016; Monsalve et al. 2017; Singh et al. 2017) or the 21-cm power spectrum (Paciga et al. 2013; Dillon et al. 2015; Jacobs et al. 2015; Beardsley et al. 2016; Patil et al. 2017; Barry et al. 2019; Gehlot et al. 2019).

Next-generation interferometric experiments, such as the Square Kilometre Array (SKA; Mellema et al. 2013) and the Hydrogen Epoch of Reionization Array (HERA; DeBoer et al. 2017), on the other hand, should be able to achieve higher signal-to-noise measurements of the spatial fluctuations across a broader frequency (redshift) range. Moreover, the SKA will provide the first three-dimensional tomographic image-cubes of the EoR and CD.

In this work, we forecast astrophysical constraints achievable with the SKA1-low.[2] In doing so, we explore several observing strategies, quantifying which one results in the best EoR/CD parameter recovery.[3] As with any 'beam-steering' instrument, different observing strategies vary the trade-off between deep/narrow versus shallow/wide observations. These change the relative balance between the two sources of 21-cm signal measurement errors: (i) cosmic (sample) variance on large spatial scales and (ii) intrinsic detector (thermal) noise on small spatial scales. Sensitivity on large spatial scales can be improved by increasing the survey volume, while the sensitivity on small scales can be improved by increasing the integration time on a single patch of sky.

What is the optimal trade-off between the two for a fixed amount of observing time? The conventional approach of judging observing (and foreground removal) strategies by their ability to recover the inputted cosmic 21-cm PS through an integrated signal to noise, assumes that astrophysical insight is encoded in 21-cm fluctuations equally on all scales. This however, is not the case. Indeed, moderately large scales ($k \sim 0.1$ Mpc^{-1}) seem more sensitive to the properties of the underlying galaxies, compared to small scales (e.g. McQuinn et al. 2007; Greig & Mesinger 2015).

The remainder of this paper is set up as follows. In Section 2, we summarize the astrophysical model used in this analysis as well as the treatment of the instrumental noise and observing strategies. In Section 3, we discuss our main finding and in Section 4, we provide our conclusions. Unless stated otherwise, we quote all quantities in co-moving units and adopt the cosmological parameters: (Ω_Λ, Ω_M, Ω_b, n, σ_8, H_0) = (0.69, 0.31, 0.048, 0.97, 0.81, 68 km s^{-1} Mpc^{-1}), consistent with recent results from the Planck mission (Planck Collaboration XIII 2016).

2 METHODOLOGY

2.1 Simulating the 21-cm signal

We simulate the cosmic 21-cm signal using the seminumerical simulation code 21CMFAST[4] (Mesinger & Furlanetto 2007; Mesinger, Furlanetto & Cen 2011). In particular, we use the most up-to-date astrophysical parametrization (Park et al. 2019), which explicitly connects the star-formation rates (SFRs) and ionizing escape fraction to the masses of the host dark matter haloes. This step enables 21CMFAST, through some simple conversions, to be able to produce UV luminosity functions (LFs) which can be compared to observed high-z galaxy LFs. Below we briefly summarize 21CMFAST and the astrophysical parametrization, and refer the reader to these aforementioned works for more details.

2.1.1 Galaxy UV properties

We assume that the typical stellar mass of a galaxy, M_*, can be related to its host halo mass, M_h (e.g. Kuhlen & Faucher-Giguère 2012; Dayal et al. 2014; Behroozi & Silk 2015; Mitra et al. 2015; Mutch et al. 2016; Sun & Furlanetto 2016; Yue, Ferrara & Xu 2016)

$$M_*(M_h) = f_* \left(\frac{\Omega_b}{\Omega_m}\right) M_h, \quad (1)$$

where f_* is the fraction of galactic gas in stars which is expressed as a power law in halo mass

$$f_* = f_{*,10} \left(\frac{M_h}{10^{10}\,M_\odot}\right)^{\alpha_*}, \quad (2)$$

with $f_{*,10}$ being the fraction of galactic gas in stars normalized to a dark matter halo of mass 10^{10} M$_\odot$ and α_* is the power-law index.[5]

Next, the SFR is estimated by dividing the stellar mass by a characteristic time-scale

$$\dot{M}_*(M_h, z) = \frac{M_*}{t_* H^{-1}(z)}, \quad (3)$$

[1] https://www.isispace.nl/projects/ncle-the-netherlands-china-low-frequency-explorer/

[2] See DeBoer et al. (2017) or Park et al. (2019) for parameter forecasts for HERA.

[3] In this work, we use the 21-cm p(PS) as a summary statistic when we compute the likelihood of a given set of parameters; however, we note that the sensitivity of the SKA should enable other, non-Gaussian probes of the cosmic 21-cm signal to be detectable (e.g. Watkinson & Pritchard 2014; Yoshiura et al. 2015; Kubota et al. 2016; Shimabukuro et al. 2016; Kakiichi et al. 2017; Shimabukuro et al. 2017; Majumdar et al. 2018; Giri et al. 2018a; Giri, Mellema & Ghara 2018b; Gorce & Pritchard 2019; Watkinson et al. 2019) which should further improve our understanding of the astrophysical processes.

[4] https://github.com/andreimesinger/21cmFAST

[5] At high redshift ($z \gtrsim 5$) this choice of a power-law dependence between stellar mass and halo mass is consistent with the mean relation from semi-analytic model predictions (e.g. Mutch et al. 2016; Yung et al. 2019) and semi-empirical fits to observations (e.g. Tacchella et al. 2018; Behroozi et al. 2019).

where $H^{-1}(z)$ is the Hubble time and t_* is a free parameter allowed to vary between zero and unity.

The UV ionizing escape fraction, $f_{\rm esc}$, is similarly allowed to vary with halo mass

$$f_{\rm esc} = f_{\rm esc,10}\left(\frac{M_{\rm h}}{10^{10}\,{\rm M}_\odot}\right)^{\alpha_{\rm esc}}, \tag{4}$$

with $f_{\rm esc,\,10}$ being normalized to a halo of mass 10^{10} M$_\odot$.

Finally, we characterize the inability of small-mass haloes to host active, star-forming galaxies (because of inefficient cooling and/or feedback), through a duty cycle

$$f_{\rm duty} = \exp\left(-\frac{M_{\rm turn}}{M_{\rm h}}\right). \tag{5}$$

In other words, a fraction $(1 - f_{\rm duty})$ of dark matter haloes of a mass $M_{\rm h}$ are unable to host star-forming galaxies, with $M_{\rm turn}$ corresponding to the characteristic scale for this suppression (e.g. Giroux, Sutherland & Shull 1994; Shapiro, Giroux & Babul 1994; Hui & Gnedin 1997; Barkana & Loeb 2001; Springel & Hernquist 2003; Mesinger & Dijkstra 2008; Okamoto, Gao & Theuns 2008; Sobacchi & Mesinger 2013a,b)

2.1.2 Galaxy X-ray properties

X-rays from stellar remnants in the first galaxies likely dominate the heating of the IGM, prior to reionization. To include the impact of X-ray heating, 21CMFAST computes a cell-by-cell angle-averaged specific X-ray intensity, $J(\boldsymbol{x}, E, z)$, (in erg s^{-1} keV^{-1} cm^{-2} sr^{-1}), by integrating the co-moving X-ray specific emissivity, $\epsilon_{\rm X}(\boldsymbol{x}, E_e, z')$ back along the light-cone

$$J(\boldsymbol{x}, E, z) = \frac{(1+z)^3}{4\pi}\int_z^\infty {\rm d}z'\frac{c\,{\rm d}t}{{\rm d}z'}\epsilon_{\rm X}{\rm e}^{-\tau}, \tag{6}$$

where $e^{-\tau}$ accounts for attenuation by the IGM. The co-moving specific emissivity, evaluated in the emitted frame, $E_{\rm e} = E(1 + z')/(1 + z)$, is,

$$\epsilon_{\rm X}(\boldsymbol{x}, E_{\rm e}, z') = \frac{L_{\rm X}}{\rm SFR}\left[(1+\bar{\delta}_{\rm nl})\int_0^\infty {\rm d}M_{\rm h}\frac{{\rm d}n}{{\rm d}M_{\rm h}}f_{\rm duty}\dot{M}_*\right], \tag{7}$$

where $\bar{\delta}_{\rm nl}$ is the mean, non-linear density in a shell around $(\boldsymbol{x}, z)$ and the quantity in square brackets is the SFR density along the light cone.

The normalization, $L_{\rm X}$/SFR (erg s^{-1} keV^{-1} $M_\odot^{-1}$ yr), is the specific X-ray luminosity per unit star formation escaping the host galaxies. It is assumed that the specific intensify follows a power law with respect to photon energy, $L_{\rm X} \propto E^{-\alpha_X}$, with photons below a threshold energy, E_0, being absorbed inside the host galaxy.[6] This specific luminosity is then normalized to the integrated soft-band (<2 keV) luminosity per SFR (in erg s^{-1} M$_\odot^{-1}$ yr), which we take to be a free parameter:

$$L_{\rm X<2\,keV}/{\rm SFR} = \int_{E_0}^{2\,{\rm keV}} {\rm d}E_{\rm e}\,L_{\rm X}/{\rm SFR}\,. \tag{8}$$

This limit of 2 keV equates to roughly the Hubble length at high redshifts, implying that harder photons do not heat the IGM (e.g. McQuinn 2012).

[6]For this work, we assume a fixed power-law slope of $\alpha_X = 1$ consistent with observations of high-mass X-ray binaries (Mineo, Gilfanov & Sunyaev 2012; Fragos et al. 2013; Pacucci et al. 2014).

2.1.3 Computing the 21-cm signal

The 21-cm signal is commonly expressed in terms of a brightness temperature contrast with respect to the CMB temperature, $T_{\rm CMB}$ (e.g. Furlanetto et al. 2006):

$$\delta T_{\rm b}(\nu) = \frac{T_{\rm S} - T_{\rm CMB}(z)}{1+z}\left(1 - {\rm e}^{-\tau_{\nu_0}}\right)\,{\rm mK}, \tag{9}$$

where τ_{ν_0} is the optical depth of the 21-cm line, which is:

$$\tau_{\nu_0} \propto (1+\delta_{\rm nl})(1+z)^{3/2}\frac{x_{\rm H\,I}}{T_{\rm S}}\left(\frac{H}{{\rm d}v_{\rm r}/{\rm d}r + H}\right). \tag{10}$$

Here, $x_{\rm H\,I}$ is the neutral hydrogen fraction, $\delta_{\rm nl} \equiv \rho/\bar{\rho} - 1$ is the gas overdensity, $H(z)$ is the Hubble parameter, ${\rm d}v_{\rm r}/{\rm d}r$ is the gradient of the line-of-sight component of the velocity and $T_{\rm S}$ is the gas spin temperature. All quantities are evaluated at redshift $z = \nu_0/\nu - 1$, where ν_0 is the 21-cm frequency and we drop the spatial dependence for brevity.

21CMFAST generates evolved density and velocity fields using second-order Lagrange perturbation theory (e.g. Scoccimarro 1998) from high resolution Gaussian initial conditions. Reionization is computed from the evolved density field by comparing the cumulative number of ionizing photons to the number of neutral hydrogen atoms plus cumulative recombinations in spheres of decreasing radii. At each cell, ionization occurs when,

$$n_{\rm ion}(\boldsymbol{x}, z|R, \delta_R) \geq (1 + \bar{n}_{\rm rec})(1 - \bar{x}_e), \tag{11}$$

where $\bar{n}_{\rm rec}$ is the cumulative number of recombinations (e.g. Sobacchi & Mesinger 2014) and $n_{\rm ion}$ is the cumulative number of IGM ionizing photons per baryon inside a spherical region of size, R and corresponding overdensity, δ_R,

$$n_{\rm ion} = \bar{\rho}_{\rm b}^{-1}\int_0^\infty {\rm d}M_{\rm h}\frac{{\rm d}n(M_h, z|R, \delta_R)}{{\rm d}M_{\rm h}}f_{\rm duty}\dot{M}_* f_{\rm esc}N_{\gamma/{\rm b}}, \tag{12}$$

where $\rho_{\rm b}$ is the mean baryon density and $N_{\gamma/{\rm b}}$ is the number of ionizing photons per stellar baryon.[7] The final term of equation (11), $(1 - \bar{x}_e)$, corresponds to the number of ionizations by X-rays, expected to contribute at a level of less than ∼10 per cent (e.g. Ricotti & Ostriker 2004; Mesinger, Ferrara & Spiegel 2013; Madau & Fragos 2017; Ross et al. 2017; Eide et al. 2018).

The temperature and the level of partial ionization of the neutral IGM is tracked in each cell, accounting for adiabatic heating/cooling, Compton heating/cooling, heating through partial ionizations, as well as the heating/ionizations from X-rays (discussed in the previous section). The spin temperature is then computed as a weighted mean between the gas and CMB temperatures, depending on the density and local Lyman α (Ly α) intensity impinging on each cell (Wouthuysen 1952; Field 1958).

This Ly α background is estimated from the summed contribution from two components (see e.g. Mesinger et al. 2011 for further details): (i) X-ray excitations of the neutral hydrogen ($J_{\alpha,\,\rm X}$) and (ii) direct stellar emission of photons between Ly α and the Lyman limit ($J_{\alpha,\,*}$). For (i) it is set by the X-ray heating rate assuming energy injection is balanced by photons redshifting out of Ly α resonance (Pritchard & Furlanetto 2007). For (ii) any absorbed Lyman n resonance photon by the neutral IGM will cascade with a recycling fraction that passes through Ly α resulting in a background that is the sum over all Lyman resonance backgrounds (e.g. Barkana & Loeb 2005). Note, currently we do not vary the soft UV spectra of

[7]We take this number to be 5000, corresponding to a Salpeter initial mass function (Salpeter 1955); however, this is highly degenerate with f_*

Table 1. Summary of the recovered precision (68 percentiles) for all the astrophysical parameters considered in this work. These include recovery of the 21-cm PS from a mock observation (parameters in top row) with observed UV LFs as an input prior. For comparison, we include the expected constraints for HERA as generated in Park et al. (2019).

	$\log_{10}(f_{*,10})$	α_*	$\log_{10}(f_{\rm esc,10})$	$\alpha_{\rm esc}$	t_*	$\log_{10}(M_{\rm turn})$ ($M_\odot$)	$\log_{10}\left(\frac{L_{X<2keV}}{SFR}\right)$ (erg s^{-1} $M_\odot^{-1}$ yr)	E_0 (keV)
Mock Obs.	−1.30	0.50	−1.00	−0.50	0.5	8.7	40.50	0.50
HERA 331 (1000 h)	$-1.20^{+0.14}_{-0.14}$	$0.47^{+0.06}_{-0.06}$	$-1.10^{+0.16}_{-0.18}$	$-0.48^{+0.14}_{-0.18}$	$0.56^{+0.21}_{-0.16}$	$8.76^{+0.19}_{-0.23}$	$40.49^{+0.05}_{-0.06}$	$0.50^{+0.03}_{-0.03}$
SKA (1000 h)	$-1.12^{+0.11}_{-0.15}$	$0.49^{+0.06}_{-0.06}$	$-1.21^{+0.16}_{-0.13}$	$-0.61^{+0.11}_{-0.13}$	$0.67^{+0.19}_{-0.19}$	$8.77^{+0.15}_{-0.19}$	$40.48^{+0.04}_{-0.04}$	$0.49^{+0.03}_{-0.03}$
SKA (10 × 100 h)	$-1.14^{+0.11}_{-0.15}$	$0.48^{+0.06}_{-0.06}$	$-1.17^{+0.16}_{-0.13}$	$-0.56^{+0.12}_{-0.15}$	$0.64^{+0.17}_{-0.18}$	$8.79^{+0.17}_{-0.19}$	$40.50^{+0.06}_{-0.06}$	$0.51^{+0.06}_{-0.04}$
SKA (100 × 10 h)	$-1.14^{+0.12}_{-0.18}$	$0.50^{+0.06}_{-0.07}$	$-1.18^{+0.20}_{-0.16}$	$-0.56^{+0.21}_{-0.22}$	$0.66^{+0.21}_{-0.22}$	$8.71^{+0.28}_{-0.30}$	$40.49^{+0.09}_{-0.09}$	$0.49^{+0.04}_{-0.04}$
No modelling uncertainty								
SKA (10 × 100 h)	$-1.23^{+0.09}_{-0.11}$	$0.47^{+0.05}_{-0.06}$	$-1.11^{+0.12}_{-0.11}$	$-0.56^{+0.09}_{-0.12}$	$0.56^{+0.15}_{-0.15}$	$8.72^{+0.14}_{-0.15}$	$40.48^{+0.05}_{-0.05}$	$0.49^{+0.05}_{-0.04}$

the first sources that produce the stellar emission component or do we consider other possible sources of soft UV (i.e. Lyα) such as quasars. We will return to this in future work.

Finally, we combine all the cosmological fields to compute the cosmic 21-cm signal, as outlined in equation (9). Additionally, we include the impact of redshift space distortions along the line of sight as outlined in Mao et al. (2012), Jensen et al. (2013), and Greig & Mesinger (2018).

2.2 Astrophysical parameter set

Under the assumption of this astrophysical model, we are left with eight free parameters, which we summarize below. We adopt the same fiducial model and allowed parameter ranges from Park et al. (2019). This model is summarized in Table 1, and its parameters are:

(i) $f_{*,10}$: normalization for the fraction of galactic gas in stars evaluated at a halo mass of 10^{10} $M_\odot$. We adopt a fiducial model of $f_{*,10} = 0.05$ and vary the log quantity as $\log_{10}(f_{*,10}) \in [-3, 0]$.

(ii) α_*: power-law index for the star formation as a function of halo mass. We adopt a fiducial value of $\alpha_* = 0.5$,[8] allowing it to vary in the range $\alpha_* \in [-0.5, 1]$.

(iii) $f_{\rm esc,10}$: normalization for the ionizing UV escape fraction evaluated at a halo mass of 10^{10} $M_\odot$. We adopt $f_{\rm esc,10} = 0.1$ to be our fiducial value, allowing it to vary in the range $f_{\rm esc,10} \in [-3, 0]$.

(iv) $\alpha_{\rm esc}$: power-law index for the ionizing UV escape fraction as a function of halo mass. We adopt a fiducial value of $\alpha_* = -0.5$, allowing it to vary in the range $\alpha_* \in [-1, 0.5]$.

(v) t_*: the star-formation time-scale as a fraction of the Hubble time. Fiducially, we adopt $t_* = 0.5$ allowing it to vary in the range $t_* \in (0, 1]$.

(vi) $M_{\rm turn}$: halo mass turnover below which the abundance of active star-forming galaxies is exponentially suppressed by the adopted duty cycle. We adopt $M_{\rm turn} = 5 \times 10^8$ $M_\odot$ to be our fiducial choice, with it being allowed to vary within the range $\log_{10}(M_{\rm turn}) \in [8, 10]$.

(vii) E_0: the minimum energy threshold for X-ray photons capable of escaping their host galaxy. We adopt a fiducial value of $E_0 = 0.5$ keV allowing it to vary within the range $E_0 \in [0.2, 1.5]$ keV. For reference, this corresponds to an integrated column density of $\log_{10}(N_{\rm H\,I}/{\rm cm}^2) \in [19.3, 23.0]$.

(viii) $L_{X<2\,keV}/SFR$: the normalization for the soft-band X-ray luminosity per unit star formation determined over the $E_0 - 2$ keV energy band. Fiducially, we adopt a value of $\log_{10}(L_{X<2\,keV}/SFR) = 40.5$, and allow it to vary in the range $\log_{10}(L_{X<2\,keV}/SFR) \in [38, 42]$.

2.3 Modelling the astrophysical noise

As we aim to explore the performance of a variety of observing strategies for the SKA1–low, we must be able to model the expected instrumental noise. Since we focus on the 21-cm PS, we use the publicly available PYTHON module 21CMSENSE[9] (Pober et al. 2013, 2014) and briefly summarize the method below.

The thermal noise PS is estimated by gridding the *uv*-visibilities according to (e.g. Morales 2005; McQuinn et al. 2006; Pober et al. 2014),

$$\Delta^2_{\rm N}(k) \approx X^2 Y \frac{k^3}{2\pi^2} \frac{\Omega'}{2t} T^2_{\rm sys}, \tag{13}$$

where X^2Y converts between observing bandwidth, frequency, and co-moving distance, Ω' is a beam-dependent factor derived in Parsons et al. (2014), t is the total time spent by all baselines within a particular k-mode and $T_{\rm sys}$ is the system temperature, the sum of the receiver temperature, $T_{\rm rec}$, and the sky temperature $T_{\rm sky}$. We model $T_{\rm sky}$ using the frequency dependent scaling $T_{\rm sky} = 60\left(\frac{\nu}{300\,{\rm MHz}}\right)^{-2.55}$ K (Thompson, Moran & Swenson 2007).

The sample (cosmic) variance contribution to the error on the inferred PS is estimated from a cosmological 21 cm PS (i.e. our fiducial mock observation of the 21-cm PS, $\Delta^2_{21}(k)^2$) and is combined with the thermal noise using an inverse-weighted summation over all the individual modes (Pober et al. 2013). This results in a total noise power, $\delta\Delta^2_{\rm T+S}(k)$, at a given Fourier mode, k,

$$\delta\Delta^2_{\rm T+S}(k) = \left(\sum_i \frac{1}{(\Delta^2_{{\rm N},i}(k) + \Delta^2_{21}(k))^2}\right)^{-\frac{1}{2}}. \tag{14}$$

Inherently, this assumes Gaussian errors for the cosmic-variance term, which for most scales is a relatively good approximation

[8]The specific choice of our fiducial parameters is somewhat arbitrary, nevertheless these result in stellar-mass to halo-mass relations that are within the typical scatter (factor of ∼2–10) shown in the literature (e.g. fig. 17 of Yung et al. 2019).

[9]https://github.com/jpober/21cmSense

(though see Mondal et al. 2015; Shaw, Bharadwaj & Mondal 2019 for more detailed discussions).

Finally, we adopt the conservative 'moderate' foreground treatment from Pober et al. (2014). This constitutes foreground avoidance, where we restrict the computation of the 21-cm PS to modes outside of the contaminated foreground 'wedge'[10] which extends $\Delta k_{\parallel} = 0.1\,h\,\mathrm{Mpc}^{-1}$ beyond the horizon limit (i.e. modes within the 'wedge' are completely removed).

2.4 SKA design and observing strategies

We estimate the SKA1–low sensitivity curves using the antennae station layout according to the recent SKA System Baseline Design document.[11] This consists of 512 35 m antennae stations randomly distributed within a 500 m core radius. The total system temperature is modelled as $T_{\rm sys} = 1.1T_{\rm sky} + 40$ K. SKA1–low is a phase-tracking experiment, for which we assume that we can conservatively perform a single six-hour track per night.

In this work, we want to explore the performance of various observing strategies for SKA. To do this, we assume a fixed survey footprint, corresponding to a total integration time of 1000 h. In principle, with the multibeaming capabilities of the SKA one could obtain two fields per observation (i.e. 2 independent 1000 h fields for the total time cost of 1000 h), however, we restrict our analysis to a single pointing for simplicity.[12] With 1000 h of integration time, we consider three possible observing strategies:

(i) deep (1000 h): A single, deep 1000 h integration of an $\sim$20 deg^2 (at 150 MHz) cold patch of sky. The SKA is primarily an imaging experiment for the EoR, thus to perform a tomographic study of the 21-cm signal the thermal noise must be minimized at the expense of cosmic variance. Thus, this strategy will be most sensitive to small spatial scales (large k-modes).

(ii) medium-deep (10×100 h): A balance between cosmic variance and thermal noise. We observe 10 independent patches of the sky for an intermediate 100 h.

(iii) Shallow (100×10 h): A shallow, but wide survey observing 100 independent patches of the sky. Minimizes the cosmic variance, reducing the noise on large scales (small k).

We note that the transformative power of the SKA will be in performing 21-cm tomography (i.e. direct imaging of the 21-cm signal) of the first billion years. For this measurement, it is important to have a good *uv*-coverage, and a high signal-to-noise ratio. Thus, regardless of its performance in parameter recovery using the PS, the deep field observation will be optimal for imaging of the 21-cm signal. This will also allow us to characterize the cosmic signal with non-Gaussian statistics (something we do not investigate here).

2.5 21CMMC setup

21CMMC is a massively parallel Monte Carlo Markov Chain (MCMC) sampler of 3D seminumerical reionization simulations (Greig & Mesinger 2015, 2017, 2018; Park et al. 2019). It is based off the PYTHON module COSMOHAMMER (Akeret et al. 2013) which uses the EMCEE PYTHON module (Foreman-Mackey et al. 2013), an affine invariant ensemble sampler from Goodman & Weare (2010). At each proposal step, 21CMMC performs an independent 3D realization of the 21-cm signal using 21CMFAST to obtain a sampled 21-cm PS. A likelihood is then estimated by comparing this sampled PS against a mock (input) PS. We calculate this likelihood over a limited k-space range of $k = 0.1$–$1.0\,\mathrm{Mpc}^{-1}$, where the lower limit is set by noise from astrophysical foregrounds while the upper limit is set by shot noise from the resolution of the simulations, respectively.

In addition to instrumental noise, we include two other sources of uncertainty. First, we adopt an uncorrelated, multiplicative modelling uncertainty of 20 per cent applied to the sampled 21-cm PS. This is motivated by approximations adopted in seminumerical simulations relative to radiative-transfer simulations (e.g. Zahn et al. 2011; Ghara et al. 2018; Hutter 2018). Secondly, we include Poisson errors on the sampled PS roughly consistent with sample variance on these scales. These two sources of uncertainty are then combined with the total noise PS from equation (14) by summing in quadrature.

In order to provide our astrophysical parameter forecasts we must construct a mock observation from which we aim to recover the input parameter values. Using the fiducial parameters outlined in Section 2.2, we construct a mock 21-cm light-cone, with a transverse scale of 500 Mpc and 256 voxels per side length. For the MCMC itself, we then sample 3D realizations of the 21-cm light-cone with a transverse scale of 250 Mpc and 128 voxels per side length. To perform the likelihood calculation, we split the 21-cm light-cone into equal 250 Mpc comoving-volume depths within which we calculate the 3D spherically averaged 21-cm PS. This results in 12 21-cm PS which span the SKA1–low frequency bandwidth, $z \sim 6$–27 (50–200 MHz).

In combination with the 21-cm PS from our mock observation, we additionally include priors from high-redshift galaxy LFs. Following Park et al. (2019), we use the $z \sim 6$ LF from Bouwens et al. (2017), $z \sim 7$–8 from Bouwens et al. (2015b) and $z \sim 10$ from Oesch et al. (2018). Including these priors enables us to improve the constraining power on the astrophysical parametrization used in this work because it breaks degeneracies amongst parameters less sensitive to the 21-cm signal (e.g. the star-formation time-scale, t_*, see Park et al. 2019 for more in-depth discussions).

3 OBSERVING-STRATEGY FORECASTS

In Fig. 1, we present the recovered one- and two-dimensional marginalized constraints for our input astrophysical model as well as the recovered UV LFs and the global evolution of the IGM neutral fraction, $\bar{x}_{\rm H\,I}$. Additionally, in Table 1, we provide the marginalized 68th percentiles for each astrophysical parameter. These correspond to the main results of this work. For reference we additionally include the astrophysical parameter constraints for a 1000 h observation with HERA from Park et al. (2019).

[10] This is a chromatic effect which arises due to how an interferometer array's *uv* coverage depends on frequency. Ideally, the frequency dependence would be completely contained along the line-of-sight ($k_{\parallel}$) direction, with the perpendicular Fourier modes ($k_{\perp}$) being frequency independent. However, this chromaticity couples $k_{\perp}$ to $k_{\parallel}$ which is more pronounced for increasing $k_{\perp}$. As a result, foreground power leaks from small-$k_{\parallel}$ into larger $k_{\parallel}$ modes for increasing $k_{\perp}$ producing a contaminated 'wedge' in cylindrical 2D k-space (Datta, Bowman & Carilli 2010; Morales et al. 2012; Parsons et al. 2012; Trott, Wayth & Tingay 2012; Vedantham, Shankar & Subrahmanyan 2012; Thyagarajan et al. 2013; Liu, Parsons & Trott 2014a,b; Thyagarajan et al. 2015b, a; Pober et al. 2016; Murray & Trott 2018).

[11] http://astronomers.skatelescope.org/wp-content/uploads/2016/09/SKA-TEL-SKO-0000422_02_SKA1_LowConfigurationCoordinates-1.pdf

[12] In practice, the nominal planned survey for the SKA (the deep survey) will cover $\sim$100 deg^2 requiring 2500 h on sky in dual-beam mode (Koopmans et al. 2015).

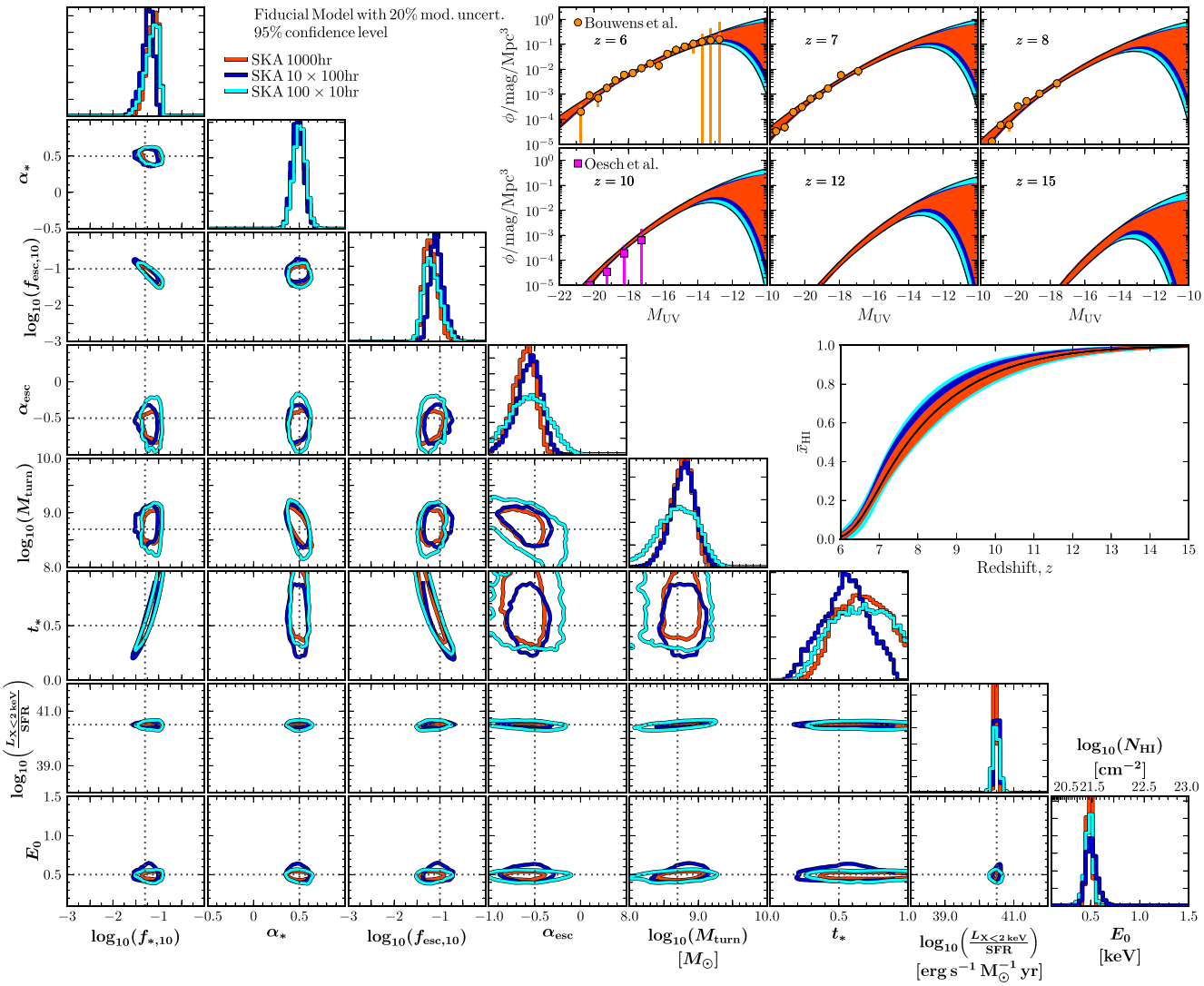

Figure 1. Recovered one- and two-dimensional marginalized contours for the astrophysical parameters for our three different observing strategies with the SKA: (i) 1000 h (deep) – red (ii) 10 × 100 h (medium-deep) – blue, and (iii) 100 × 10 h (shallow) – cyan. For all, we include the 20 per cent modelling uncertainty. Black dotted lines correspond to the input fiducial model parameters. Top right panels are the recovered 95 percentiles on the UV LFs at several redshifts compared to the input observed LFs (used as observational priors and represented by the orange and pink data points). Middle right corresponds to the global evolution of the IGM neutral fraction, $\bar{x}_{\rm H\,I}$.

3.1 Comparing observing strategies

Surprisingly, for the majority of the astrophysical parameters, all three observing strategies perform equally well. Note that for the X-ray parameters, there is no distinguishable difference between the strategies. However, for $\alpha_{\rm esc}$, $M_{\rm turn}$, and t_* the largest differences occur. Thus, the observing strategies have the largest impact on the galaxy UV properties. First, it is immediately obvious that the shallow (100 × 10 h) survey incurs the largest errors. This is equally reflected in the broader recovered UV LFs and reionization history. Clearly, by focussing on the largest scales (smallest k-modes), constraining information is lost from the intermediate to smaller scales (larger k-modes) where thermal noise dominates. Note though that we restrict our likelihood fitting to $k = 0.1$–1.0 Mpc^{-1}. If this lower bound could be reduced (requiring observing into the foreground wedge) the relative performance of the shallow survey would be improved as it is most sensitive to modes within the foreground 'wedge'.

On the other hand, the deep (1000 h) and medium-deep (10 × 100 h) surveys result in comparable constraints. To highlight these similarities, we cast the 68th percentiles as approximate 1σ uncertainties. In doing so, we find [$\log_{10}(f_{*,10})$, α_*, $\log_{10}(f_{\rm esc,10})$, $\alpha_{\rm esc}$, t_*, $\log_{10}(M_{\rm turn})$, E_0, $\log_{10}(L_{X<2\,\rm keV}/\rm SFR)$] = (11.6, 12.2, 12.0, 19.7, 28.4, 1.9, 0.1, 6.1) per cent for the deep scenario and (11.4, 12.3, 12.4, 24.0, 27.3, 2.0, 0.1, 9.8) per cent for the medium-deep scenario.

For the star-formation time-scale, t_*, the medium-deep strategy recovers notably tighter constraints as highlighted by the one-dimensional marginalized histogram for t_*. However, the deep survey strategy recovers marginally tighter UV LFs and reionization history. These differences arise mostly from the degeneracies between t_*–$f_{\rm esc,10}$ and t_*–$f_{*,10}$. Notably, for the deep survey all three quantities are slightly offset from their expected fiducial value unlike that for the medium-deep strategy. This slight offset in these parameters from the deep survey in combination with the tighter t_*

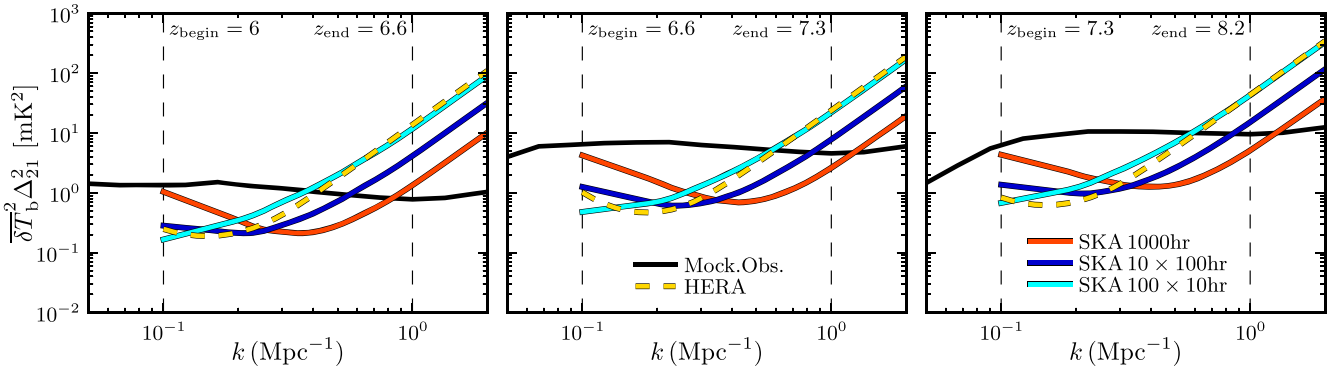

Figure 2. A comparison of the sensitivity curves for the three different SKA observing strategies. The black curve corresponds to the spherically averaged 21-cm power spectrum for the first three equal comoving chunks of the 21-cm light cones whereas the red, blue, and cyan curves are the sensitivity curves for the 1000 h (deep), 10 × 100 h (medium-deep), and 100 × 10 h (shallow) strategies, respectively. The yellow dashed curve corresponds to the HERA 331 sensitivity curve. The vertical black dashed lines correspond to our adopted fitting range for estimating the likelihood (see e.g. Section 2.5).

constraints for the medium-deep scenario indicates that the medium-deep strategy is the preferred observing strategy. The source of this slight offset likely arises from two correlated sources: (i) how the sensitivity for each strategy is distributed over k-space for the 21-cm PS and (ii) that the fiducial galaxy UV parameters were not *a priori* selected to be an exact match to the input observational priors (UV LFs). For the former, in Fig. 2 we compare the sensitivity curves of each strategy for the first three equal comoving chunks from the 21-cm light-cone of the mock observation. The deep strategy (red curve) prefers the smallest scales (large k-modes), whereas the medium-deep (blue curve) scenario pushes further into the large-scale modes. We anticipate the largest scales to be the most sensitive to the astrophysical information, thus a more uniform distribution of noise from the medium-deep strategy over k-space will improve the astrophysical parameter recovery. For the latter, the best recovered UV parameters from the UV LFs alone differ from those recovered from the 21-cm PS. Coupling this with differences in the sensitivity per k-mode will cause slight offsets when the 21-cm PS recovery is less sensitive as shown in Park et al. (2019).

It is important to remember here that we only use the 21-cm PS to compute the likelihood. Additionally including non-Gaussian statistics (e.g. Watkinson & Pritchard 2014; Yoshiura et al. 2015; Kubota et al. 2016; Shimabukuro et al. 2016; Kakiichi et al. 2017; Shimabukuro et al. 2017; Shimabukuro & Semelin 2017; La Plante & Ntampaka 2018; Majumdar et al. 2018; Giri et al. 2018a; Giri et al. 2018b; Gillet et al. 2019; Gorce & Pritchard 2019; Hassan et al. 2019; Watkinson et al. 2019) would improve the relative performance of the deep survey, as it has the largest signal to noise for higher order statistics.

3.2 Comparison to HERA

Finally, in Table 1, we compare the astrophysical forecasts from SKA to those for a 1000 h observation from HERA explored in Park et al. (2019). Note, in both instances we only use the PS space above the wedge.[13] Again, we caution that this is not a direct like-for-like comparison as HERA is a drift scan observation compared to the tracked scanning to be performed by the SKA. Thus, HERA will have better sensitivity on larger scales owing to reduced sample variance (i.e. more independent observing fields) at the expense of small-scale sensitivity owing to increased thermal noise (see e.g. Fig. 2). Nevertheless, we find that the medium-deep observing strategy marginally outperforms HERA as evidenced by the slightly reduced fractional errors on the recovered astrophysical parameters. We note, however, that SKA aims to remove the foregrounds (Koopmans et al. 2015) and utilize the full PS space inside the wedge as well, potentially significantly increasing its power to recover astrophysical parameters (DeBoer et al. 2017). Approximating these percentiles as 1σ fractional errors we find $[\log_{10}(f_{*,10})$, α_*, $\log_{10}(f_{\rm esc,10})$, $\alpha_{\rm esc}$, t_*, $\log_{10}(M_{\rm turn})$, E_0, $\log_{10}(L_{\rm X<2keV}/{\rm SFR})]$ = (11.4, 12.3, 12.4, 24.0, 27.3, 2.0, 0.1, 9.8) per cent for the SKA and (11.7, 12.8, 15.5, 33.3, 33.0, 2.4, 0.1, 6.0) for HERA. Note again though that offsets arise in the median recovered astrophysical parameters relative to the fiducial parameters. However, these again can be attributed to the combined effect of the instrumental sensitivity on different k-scales and the chosen input UV LFs not preferring the same fiducial galaxy UV parameters as the mock observation.

3.3 Impact of modelling uncertainty

Throughout this work we have included an additional 20 per cent modelling uncertainty to our estimation of the likelihood. However, it is useful to explore the idealized case that modelling errors can be efficiently characterized and accounted for. Thus in Fig. 3 and summarized at the bottom of Table 1, we compare our best-performing observing strategy, the medium-deep survey, with and without this modelling uncertainty.

Approximating the marginalized PDFs to obtain simplified 1σ fractional errors, we find $[\log_{10}(f_{*,10})$, α_*, $\log_{10}(f_{\rm esc,10})$, $\alpha_{\rm esc}$, t_*, $\log_{10}(M_{\rm turn})$, E_0, $\log_{10}(L_{\rm X<2keV}/{\rm SFR})]$ = (11.4, 12.3, 12.4, 24.0, 27.3, 2.0, 0.1, 9.8) per cent for the medium-deep scenario with the modelling uncertainty compared to (8.1, 11.7, 10.4, 18.8, 26.8, 1.7, 0.1, 9.2) without the modelling uncertainty. Thus, including a 20 per cent modelling uncertainty increases the fractional uncertainties by (40.7, 5.1, 19.2, 27.7, 1.9, 18.0, 20.0, 6.5) per cent. The largest improvement in the recovery is for the star formation time-scale parameter. However, in general, assuming no modelling error does not improve the recovery dramatically, suggesting that it is not the largest source of uncertainty, for this mock observation.

[13] In using 21CMSENSE we ensure that the shape of the foreground wedge is appropriately taken into account for each instrument as it uses the specific layout configuration for each instrument. Further, 21CMSENSE also takes into account redundant baselines, which is a feature of HERA.

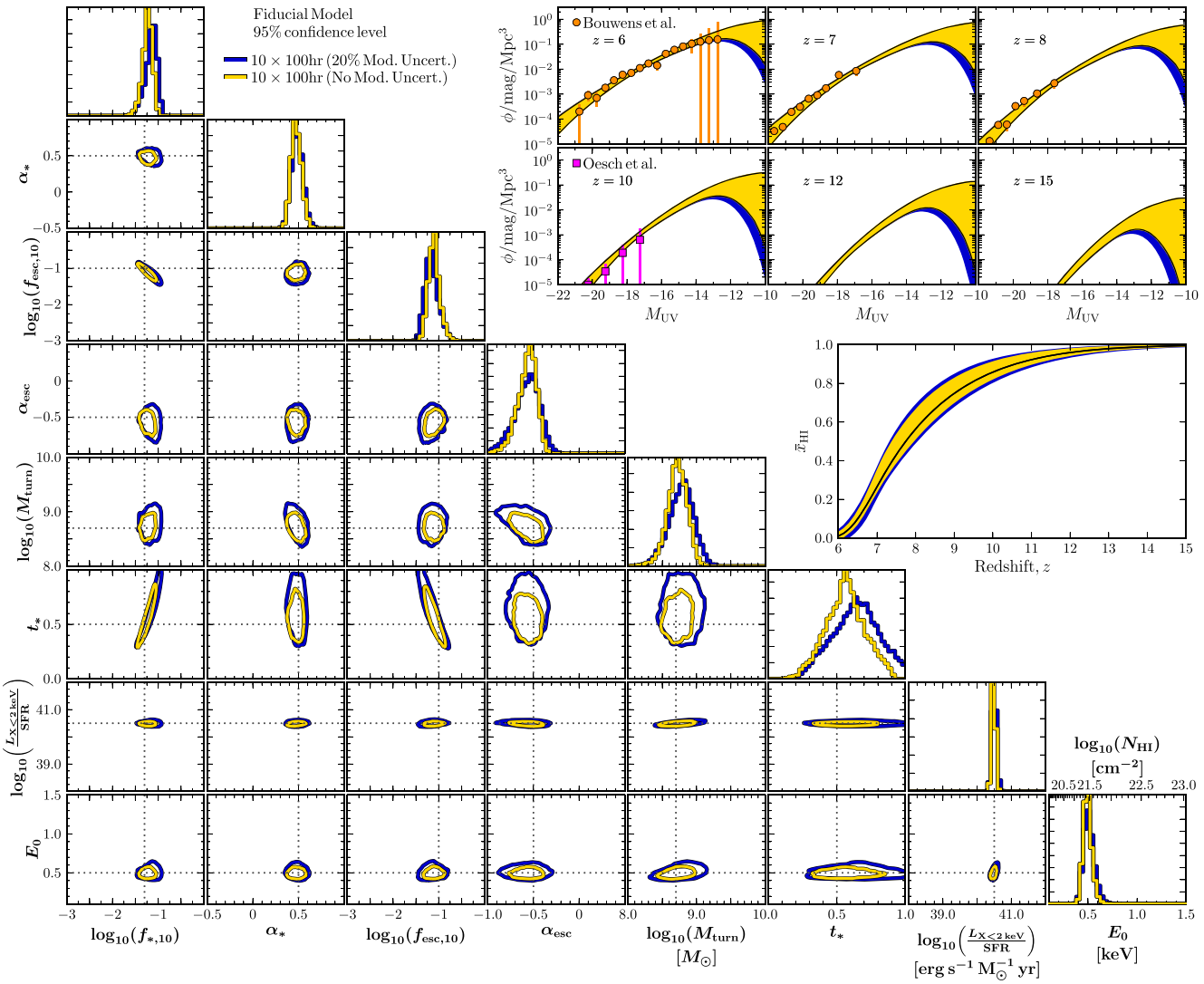

Figure 3. Same as Fig. 1 except now we compare the impact of the modelling uncertainty on the 10 × 100 h (medium-deep) observing strategy: (i) 20 per cent modelling uncertainty – blue and (ii) no modelling uncertainty – yellow.

4 CONCLUSION

The ultimate goal for current and future reionization experiments is to recover a full three-dimensional view of the early Universe through detection of the 21-cm signal of neutral hydrogen. In doing so, we will be able to obtain insights into the formation and nature of the first stars and galaxies along with their growth over the first billion years.

The most ambitious upcoming 21-cm telescope is the SKA. Here we provide EoR/CD astrophysical parameter forecasts achievable with SKA1-low under some very conservative assumptions: (i) that only the EoR window above the foreground wedge is used and (ii) 20 per cent modelling uncertainties are included. We use a physically motivated galaxy formation model which allows us to make use of observed LFs of high-z galaxies, in addition to mock SKA 21-cm PS measurements.

We consider three different SKA observing strategies, quantifying the trade-off between minimizing the errors associated with cosmic (sample) variance and instrumental (thermal) noise. For a fixed total integration time, we considered: (i) a deep 1000 h observation of a single patch of sky (ii) a medium-deep 100 h observation of 10 independent fields, and (iii) a shallow 10 h observation of 100 independent fields. We note that the SKA aims to observe about five times this volume (Koopmans et al. 2015).

Under the above assumptions, we find that the deep and medium-deep observing strategies perform almost equally well, both yielding tighter parameter constraints compared with the shallow strategy. Approximated as 1σ uncertainties the medium-deep survey recovers the following constraints: [$\log_{10}(f_{*,10})$, α_*, $\log_{10}(f_{\rm esc,10})$, $\alpha_{\rm esc}$, t_*, $\log_{10}(M_{\rm turn})$, E_0, $\log_{10}(L_{\rm X<2\,keV}/{\rm SFR})$] = (11.4, 12.3, 12.4, 24.0, 27.3, 2.0, 0.1, 9.8) per cent.

Additionally, we explore the impact of our chosen 20 per cent modelling uncertainty on our recovered astrophysical parameters. We find that an optimistic scenario in which the modelling error can be completely corrected for, only modestly improves parameter constraints (at most tens of per cent). Thus, a modelling error at the level of a few tens of per cent does not strongly degrade the accuracy of parameter recovery, for our galaxy formation model. With SKA1-low we therefore will be able to recover the astrophysics of reionization and the CD at the level of ∼10 per cent, or better.

ACKNOWLEDGEMENTS

We thank the anonymous referee for their comments. Parts of this research were supported by the Australian Research Council Centre of Excellence for All Sky Astrophysics in 3 Dimensions (ASTRO 3D), through project number CE170100013. AM acknowledges funding support from the European Research Council (ERC) under the European Union's Horizon 2020 research and innovation programme (grant agreement No 638809 – AIDA – PI: AM). The results presented here reflect the authors' views; the ERC is not responsible for their use. LVEK acknowledges support from a SKA-NL Roadmap grant from the Dutch ministry of OCW.

REFERENCES

Akeret J., Seehars S., Amara A., Refregier A., Csillaghy A., 2013, Astron. Comput., 2, 27
Barkana R., Loeb A., 2001, Phys. Rep., 349, 125
Barkana R., Loeb A., 2005, ApJ, 626, 1
Barry N. et al., 2019, ApJ, 884, 1
Beardsley A. P. et al., 2016, ApJ, 833, 102
Behroozi P. S., Silk J., 2015, ApJ, 799, 32
Behroozi P., Wechsler R. H., Hearin A. P., Conroy C., 2019, MNRAS, 488, 3143
Bernardi G. et al., 2016, MNRAS, 461, 2847
Bowman J. D., Rogers A. E. E., 2010, Nature, 468, 796
Bouwens R. J., Illingworth G. D., Oesch P. A., Caruana J., Holwerda B., Smit R., Wilkins S., 2015a, ApJ, 811, 140
Bouwens R. J. et al., 2015b, ApJ, 803, 34
Bouwens R. J., Oesch P. A., Illingworth G. D., Ellis R. S., Stefanon M., 2017, ApJ, 843, 129
Bowman J. D., Rogers A. E. E., Monsalve R. A., Mozdzen T. J., Mahesh N., 2018a, Nature, 555, 67
Bowman J. D., Rogers A. E. E., Monsalve R. A., Mozdzen T. J., Mahesh N., 2018b, Nature, 564, E35
Bradley R. F., Tauscher K., Rapetti D., Burns J. O., 2019, ApJ, 874, 153
Datta A., Bowman J. D., Carilli C. L., 2010, ApJ, 724, 526
Dayal P., Ferrara A., Dunlop J. S., Pacucci F., 2014, MNRAS, 445, 2545
DeBoer D. R. et al., 2017, PASP, 129, 045001
Dillon J. S. et al., 2015, Phys. Rev. D, 91, 123011
Draine B. T., Miralda-Escudé J., 2018, ApJ, 858, L10
Eide M. B., Graziani L., Ciardi B., Feng Y., Kakiichi K., Di Matteo T., 2018, MNRAS, 476, 1174
Field G. B., 1958, Proc. Inst. Radio Eng., 46, 240
Foreman-Mackey D., Hogg D. W., Lang D., Goodman J., 2013, PASP, 125, 306
Fragos T. et al., 2013, ApJ, 764, 41
Furlanetto S. R., Oh S. P., Briggs F. H., 2006, Phys. Rep., 433, 181
Gardner J. P. et al., 2006, Space Sci. Rev., 123, 485
Gehlot B. K. et al., 2019, MNRAS, 488, 4271
Ghara R., Mellema G., Giri S. K., Choudhury T. R., Datta K. K., Majumdar S., 2018, MNRAS, 476, 1741
Gillet N., Mesinger A., Greig B., Liu A., Ucci G., 2019, MNRAS, 484, 282
Giri S. K., Mellema G., Dixon K. L., Iliev I. T., 2018a, MNRAS, 473, 2949
Giri S. K., Mellema G., Ghara R., 2018b, MNRAS, 479, 5596
Giroux M. L., Sutherland R. S., Shull J. M., 1994, ApJ, 435, L97
Gnedin N. Y., Ostriker J. P., 1997, ApJ, 486, 581
Gnedin N. Y., Shaver P. A., 2004, ApJ, 608, 611
Goodman J., Weare J., 2010, Commun. Appl. Math. Comput. Sci., 5, 1
Gorce A., Pritchard J. R., 2019, MNRAS, 489, 1321
Greenhill L. J., Bernardi G., 2012, preprint (arXiv:1201.1700)
Greig B., Mesinger A., 2015, MNRAS, 449, 4246
Greig B., Mesinger A., 2017, MNRAS, 472, 2651
Greig B., Mesinger A., 2018, MNRAS, 477, 3217
Hassan S., Liu A., Kohn S., La Plante P., 2019, MNRAS, 483, 2524
Hills R., Kulkarni G., Meerburg P. D., Puchwein E., 2018, Nature, 564, E32
Hui L., Gnedin N. Y., 1997, MNRAS, 292, 27
Hutter A., 2018, MNRAS, 477, 1549
Jacobs D. C. et al., 2015, Nature, 801, 51
Jensen H. et al., 2013, MNRAS, 435, 460
Kakiichi K. et al., 2017, MNRAS, 471, 1936
Koopmans L. et al., 2015, Proc. Sci, The Cosmic Dawn and Epoch of Reionisation with SKA. SISSA, Trieste, PoS#1
Kubota K., Yoshiura S., Shimabukuro H., Takahashi K., 2016, PASJ, 68, 61
Kuhlen M., Faucher-Giguère C.-A., 2012, MNRAS, 423, 862
La Plante P., Ntampaka M., 2019, ApJ, 880, 110
Liu A., Parsons A. R., Trott C. M., 2014a, Phys. Rev. D, 90, 023018
Liu A., Parsons A. R., Trott C. M., 2014b, Phys. Rev. D, 90, 023019
Madau P., Fragos T., 2017, ApJ, 840, 39
Madau P., Meiksin A., Rees M. J., 1997, ApJ, 475, 429
Majumdar S., Pritchard J. R., Mondal R., Watkinson C. A., Bharadwaj S., Mellema G., 2018, MNRAS, 476, 4007
Mao Y., Shapiro P. R., Mellema G., Iliev I. T., Koda J., Ahn K., 2012, MNRAS, 422, 926
McQuinn M., 2012, MNRAS, 426, 1349
McQuinn M., Zahn O., Zaldarriaga M., Hernquist L., Furlanetto S. R., 2006, ApJ, 653, 815
McQuinn M., Lidz A., Zahn O., Dutta S., Hernquist L., Zaldarriaga M., 2007, MNRAS, 377, 1043
Mellema G. et al., 2013, Exp. Astron., 36, 235
Mesinger A., Dijkstra M., 2008, MNRAS, 390, 1071
Mesinger A., Furlanetto S., 2007, ApJ, 669, 663
Mesinger A., Furlanetto S., Cen R., 2011, MNRAS, 411, 955
Mesinger A., Ferrara A., Spiegel D. S., 2013, MNRAS, 431, 621
Mineo S., Gilfanov M., Sunyaev R., 2012, MNRAS, 419, 2095
Mitra S., Choudhury T. R., Ferrara A., 2015, MNRAS, 454, L76
Mondal R., Bharadwaj S., Majumdar S., Bera A., Acharyya A., 2015, MNRAS, 449, L41
Monsalve R. A., Rogers A. E. E., Bowman J. D., Mozdzen T. J., 2017, ApJ, 847, 64
Morales M. F., 2005, ApJ, 619, 678
Morales M. F., Wyithe J. S. B., 2010, ARA&A, 48, 127
Morales M. F., Hazelton B., Sullivan I., Beardsley A., 2012, ApJ, 752, 137
Murray S. G., Trott C. M., 2018, ApJ, 869, 25
Mutch S. J., Geil P. M., Poole G. B., Angel P. W., Duffy A. R., Mesinger A., Wyithe J. S. B., 2016, MNRAS, 462, 250
Oesch P. A., Bouwens R. J., Illingworth G. D., Labbé I., Stefanon M., 2018, ApJ, 855, 105
Okamoto T., Gao L., Theuns T., 2008, MNRAS, 390, 920
Paciga G. et al., 2013, MNRAS, 433, 1174
Pacucci F., Mesinger A., Mineo S., Ferrara A., 2014, MNRAS, 443, 678
Park J., Mesinger A., Greig B., Gillet N., 2019, MNRAS, 484, 933
Parsons A. R. et al., 2010, AJ, 139, 1468
Parsons A. R., Pober J. C., Aguirre J. E., Carilli C. L., Jacobs D. C., Moore D. F., 2012, ApJ, 756, 165
Parsons A. R. et al., 2014, ApJ, 788, 106
Patil A. H. et al., 2017, ApJ, 838, 65
Patra N., Subrahmanyan R., Sethi S., Shankar N. U., Raghunathan A., 2015, ApJ, 801, 138
Philip L. et al., 2019, J. Astron. Instrum., 8, 1950004
Planck Collaboration XIII, 2016, A&A, 594, A13
Pober J. C. et al., 2013, AJ, 145, 65
Pober J. C. et al., 2014, ApJ, 782, 66
Pober J. C. et al., 2016, ApJ, 819, 8
Pritchard J. R., Furlanetto S. R., 2007, MNRAS, 376, 1680
Pritchard J. R., Loeb A., 2012, Rep. Prog. Phys., 75, 086901
Ricotti M., Ostriker J. P., 2004, MNRAS, 350, 539
Ross H. E., Dixon K. L., Iliev I. T., Mellema G., 2017, MNRAS, 468, 3785
Salpeter E. E., 1955, ApJ, 121, 161
Scoccimarro R., 1998, MNRAS, 299, 1097
Shapiro P. R., Giroux M. L., Babul A., 1994, ApJ, 427, 25
Shaver P. A., Windhorst R. A., Madau P., de Bruyn A. G., 1999, A&A, 345, 380
Shaw A. K., Bharadwaj S., Mondal R., 2019, MNRAS, 487, 4951
Shimabukuro H., Semelin B., 2017, MNRAS, 468, 3869

Shimabukuro H., Yoshiura S., Takahashi K., Yokoyama S., Ichiki K., 2016, MNRAS, 458, 3003
Shimabukuro H., Yoshiura S., Takahashi K., Yokoyama S., Ichiki K., 2017, MNRAS, 468, 1542
Singh S., Subrahmanyan R., 2019, ApJ, 880, 26
Singh S. et al., 2017, ApJ, 845, L12
Sobacchi E., Mesinger A., 2013a, MNRAS, 432, L51
Sobacchi E., Mesinger A., 2013b, MNRAS, 432, 3340
Sobacchi E., Mesinger A., 2014, MNRAS, 440, 1662
Sokolowski M. et al., 2015, Publ. Astron. Soc. Aust., 32, e004
Springel V., Hernquist L., 2003, MNRAS, 339, 312
Sun G., Furlanetto S. R., 2016, MNRAS, 460, 417
Tacchella S., Bose S., Conroy C., Eisenstein D. J., Johnson B. D., 2018, ApJ, 868, 92
Thompson A. R., Moran J. M., Swenson G. W., 2007, in Interferometry and Synthesis in Radio Astronomy. Wiley, New York
Thyagarajan N. et al., 2013, ApJ, 776, 6
Thyagarajan N. et al., 2015a, ApJ, 807, L28
Thyagarajan N. et al., 2015b, ApJ, 804, 14
Tingay S. J. et al., 2013, Publ. Astron. Soc. Aust., 30, e007
Tozzi P., Madau P., Meiksin A., Rees M. J., 2000, ApJ, 528, 597
Trott C. M., Wayth R. B., Tingay S. J., 2012, ApJ, 757, 101
van Haarlem M. P. et al., 2013, A&A, 556, A2
Vedantham H., Shankar N. U., Subrahmanyan R., 2012, ApJ, 745, 176
Voytek T. C., Natarajan A., García J. M. J., Peterson J. B., López-Cruz O., 2014, ApJ, 782, L9
Watkinson C. A., Pritchard J. R., 2014, MNRAS, 443, 3090
Watkinson C. A., Giri S. K., Ross H. E., Dixon K. L., Iliev I. T., Mellema G., Pritchard J. R., 2019, MNRAS, 482, 2653
Wouthuysen S. A., 1952, AJ, 57, 31
Yatawatta S. et al., 2013, A&A, 550, A136
Yoshiura S., Shimabukuro H., Takahashi K., Momose R., Nakanishi H., Imai H., 2015, MNRAS, 451, 266
Yue B., Ferrara A., Xu Y., 2016, MNRAS, 463, 1968
Yung L. Y. A., Somerville R. S., Popping G., Finkelstein S. L., Ferguson H. C., Davé R., 2019, MNRAS, 490, 2855
Zahn O., Mesinger A., McQuinn M., Trac H., Cen R., Hernquist L. E., 2011, MNRAS, 414, 727

This paper has been typeset from a TEX/LATEX file prepared by the author.